Annals of Biomedical Engineering, Vol. 38, No. 1, January 2010 *(© 2009)* pp. 138–157
DOI: 10.1007/s10439-009-9840-9

Fast and Accurate Registration Techniques for Affine and Nonrigid Alignment of MR Brain Images

JIA-XIU LIU,[1] YONG-SHENG CHEN,[1] and LI-FEN CHEN[2]

[1]Department of Computer Science, National Chiao Tung University, 1001 University Road, Hsinchu 300, Taiwan; and [2]Institute of Brain Science, National Yang-Ming University, No. 155, Sec. 2, Linong Street, Taipei 112, Taiwan

(Received 6 March 2009; accepted 6 November 2009; published online 20 November 2009)

Abstract—Registration of magnetic resonance brain images is a geometric operation that determines point-wise correspondences between two brains. It remains a difficult task due to the highly convoluted structure of the brain. This paper presents novel methods, Brain Image Registration Tools (BIRT), that can rapidly and accurately register brain images by utilizing the brain structure information estimated from image derivatives. Source and target image spaces are related by affine transformation and non-rigid deformation. The deformation field is modeled by a set of Wendland's radial basis functions hierarchically deployed near the salient brain structures. In general, nonlinear optimization is heavily engaged in the parameter estimation for affine/non-rigid transformation and good initial estimates are thus essential to registration performance. In this work, the affine registration is initialized by a rigid transformation, which can robustly estimate the orientation and position differences of brain images. The parameters of the affine/non-rigid transformation are then hierarchically estimated in a coarse-to-fine manner by maximizing an image similarity measure, the correlation ratio, between the involved images. T1-weighted brain magnetic resonance images were utilized for performance evaluation. Our experimental results using four 3-D image sets demonstrated that BIRT can efficiently align images with high accuracy compared to several other algorithms, and thus is adequate to the applications which apply registration process intensively. Moreover, a voxel-based morphometric study quantitatively indicated that accurate registration can improve both the sensitivity and specificity of the statistical inference results.

Keywords—Affine/non-rigid image registration, Difference of Gaussian, Radial basis functions, Correlation ratio, Voxel-based morphometry.

INTRODUCTION

Registration is an essential geometric operation in medical image analysis. In longitudinal studies, for instance, images acquired repeatedly over a period of time can be used to observe the temporal changes of brain structures by subtracting the registered images[32,53] or by analyzing the structure deformation.[72,59] Customized or standard brain templates can be constructed by spatially normalizing and then averaging the brain images in a stereotaxic space.[28,29,51,52] Registration of an individual brain to the template can bridge the individual brain to the Talairach space[70] and can also help to obtain the gross anatomical structures of the individual brain with template-based segmentation methods.[24,26]

When registering images, the degree of structural variability determines the transformation model to be adopted. Rigid or affine transformation can only accommodate the global transformation and are adequate to register the images acquired for the same subject. Many approaches were proposed for affine registration of brain images. Ashburner *et al.* incorporated the prior knowledge of human brains into a Bayesian framework.[10] Wood *et al.* used a Newton-type method to iteratively optimize the values of transformation parameters.[79] Jenkinson *et al.* proposed a coarse-to-fine method that can optimize the transformation parameters from multiple candidates.[38,39]

A transformation model with a high degree of freedom is indispensable to inter-subject registration, in which the anatomical difference is non-rigid. In the following, non-rigid registration methods are briefly introduced according to the adopted transformation model. Comprehensive surveys can be found in references.[33,37,57,83]

Elastic methods register images by compromising the deformation smoothness and the similarity measurement between images.[11] Because of the smoothness constraint, these kinds of methods may not sufficiently model highly localized deformation, such as the convolution of cerebral cortex.[45,62] Their variants, fluid models, relax the smoothness constraint to overcome this problem at a higher risk of false registration.[45]

Address correspondence to Li-Fen Chen, Institute of Brain Science, National Yang-Ming University, No. 155, Sec. 2, Linong Street, Taipei 112, Taiwan. Electronic mail: jsliu@csie.nctu.edu.tw, yschen@cs.nctu.edu.tw, lfchen@ym.edu.tw

0090-6964/10/0100-0138/0 © 2009 Biomedical Engineering Society

Fluid registration works can be found in references.[16,21,32] Moreover, the Demons algorithm[71] and its variant[75] are also considered as an approximation of fluid registration.[33]

A finite element method (FEM) registers images by using the segmented objects, which are usually represented by the meshes of tetrahedrons or hexahedrons.[6,27,30,65,66,77,81] It can deform objects in a more realistic way because different energy terms can be assigned to objects according to their physical properties. However, the computational complexity of the FEM approach is generally high and the error of tissue segmentation contributes to the deviation of registration.

Basis functions have been extensively applied to describe the spatial mapping relationship between images. These methods can be further divided into two sub-categories. The first kind of methods, referred as landmark-based approaches, establishes the spatial transformation from a set of corresponding control points or landmarks. Numerous basis functions have been used to model the spatial mapping, such as the thin-plate splines (TPS),[13,47] Gaussian,[2] inverse multi-quadrics,[64] multi-quadrics,[47] and Wendland's radial basis functions (RBFs).[31] The major disadvantage of these kinds of methods is that the identification of landmarks is not only time-consuming but also prone to errors. To alleviate this problem, Likar and Pernus applied affine registration to the sub-regions of images and regarded the centers of the registered parts as the matching control points.[46]

Instead of the labor-intensive landmark selection, the second kind of methods regularly deploy basis functions in image volumes and calculate the coefficients of basis functions by optimizing an objective function. Many basis functions have been applied to model the deformation fields, including wavelets,[1] discrete cosine transform,[7] and B-splines.[44,63] However, a large number of basis functions are required to model subtle deformation. In this case, the computational complexity is high and it is usually difficult to obtain good results by searching in a large parameter space. To reduce the number of basis functions, Rohde *et al.* used the gradient magnitude of the normalized mutual information (NMI) to detect poorly aligned image regions and repeatedly deployed RBFs in these regions for registration refinement.[61]

Anatomical information has also been applied in non-rigid registration frameworks. Pluim *et al.* incorporated image gradient into the similarity measurement, mutual information (MI), for utilizing the spatial information.[55] Marsland *et al.* iteratively determined the poorly registered regions and deployed knot points to the strong edges for modeling the deformation field with the clamped-plate splines.[50] Camara *et al.* registered the corresponding structures and used the obtained results to initialize the subsequent procedure for the multimodal registration of whole-body images.[18] More examples can be found in references.[17,36,42,48,74] Generally, these type of methods take advantage of both the structure and intensity information during the registration process.

Image registration is an important tool in quantitative analysis using voxel-based morphometry (VBM). VBM statistically reveals the structural differences between two image groups through a voxel-wise comparison of tissue volumes.[8] There have been numerous VBM studies presented in the literature, such as the examination of brain asymmetry and the effects of sex and handedness in brain structures,[35] the aging of brains,[34] and the characterization of diseases.[12,15,41] Before the statistical comparison, all images have to be spatially normalized into the same stereotaxic space such that the corresponding structures are well aligned. Many registration techniques have been adopted in the VBM procedure and the accuracy of image registration can greatly affect the reliability of the analysis results.[3,9,14,22] Moreover, VBM analysis usually applies registration procedure intensively. Therefore, an accurate and time efficient registration algorithm is generally considered preferable for VBM.

In this work, we utilize the structure information of the brain extracted from image derivatives and develop affine and non-rigid methods, called the Brain Image Registration Tools (BIRT), for the accurate and time efficient registration of magnetic resonance (MR) brain images. The proposed affine method aligns brain images by estimating the orientation and position differences between brains followed by optimizing the similarity between images in a hierarchical manner. The non-rigid deformation of the brain is modeled by a set of Wendland's RBFs, which are hierarchically deployed near the salient anatomical structures. In this way, a small amount of RBFs are sufficient to well represent the deformation field and thus are beneficial to the execution efficiency. A VBM study of inter-group structural analysis is also conducted to qualitatively and quantitatively investigate the effect of registration accuracy upon the VBM analysis results. Software packages of the proposed registration algorithms are available at http://bsp.cs.nctu.edu.tw/software.

METHODS

Image registration establishes the spatial mapping $\mathbf{T} : \mathbf{p} \mapsto \mathbf{q}$, which transforms every point $\mathbf{p}$ in the source (or test) image to its corresponding point $\mathbf{q}$ in the target

(or reference) image, such that the same structures are well aligned. The mapping relation $\mathbf{T}$ generally consists of a global transformation $\mathbf{T}_g$, which is usually an affine transformation, and a local, non-rigid deformation $\mathbf{T}_l$:

$$\mathbf{q} = \mathbf{T}(\mathbf{p}) = \mathbf{T}_g(\mathbf{p}) + \mathbf{T}_l(\mathbf{T}_g(\mathbf{p})). \quad (1)$$

Notice that $\mathbf{T}_g$ maps each point $\mathbf{p}$ to its corresponding point $\mathbf{T}_g(\mathbf{p})$ while $\mathbf{T}_l$ represents the non-rigid displacement vector field. This section first introduces how to extract the structure information of the brain from image derivatives and then presents the proposed affine and non-rigid registration methods based on the extracted information.

Structure Information of the Brain

Difference of Gaussian (DOG) performs image subtraction after convolution with two Gaussian kernels $G(\sigma_1)$ and $G(\sigma_2)$, $\sigma_1 > \sigma_2$:

$$\mathrm{DOG}(I, \sigma_1, \sigma_2) = G(\sigma_1) * I - G(\sigma_2) * I, \quad (2)$$

where I is a T1-weighted MR image and "*" denotes the convolution operator. We define the thresholded DOG (TDOG) value to be one (foreground) when the DOG value is larger than a threshold, and otherwise the TDOG value is zero (background). Instead of using the zero-crossings of DOG results to detect edge features, we utilize the foreground in the TDOG image to reveal those regions with relatively low intensity in I, such as the gray matter (GM) and cerebrospinal fluid (CSF), as shown in Fig. 1. Notice that the region between two hemispheres contains mostly TDOG foreground voxels. This phenomenon can be utilized to determine the mid-sagittal planes (MSPs) and then estimate the orientation of brains. Non-brain tissues may present in TDOG foreground and can be easily removed by applying the brain masks. Then the masked foreground can guide the deployment of RBFs to cortices and ventricles in the proposed non-rigid registration method.

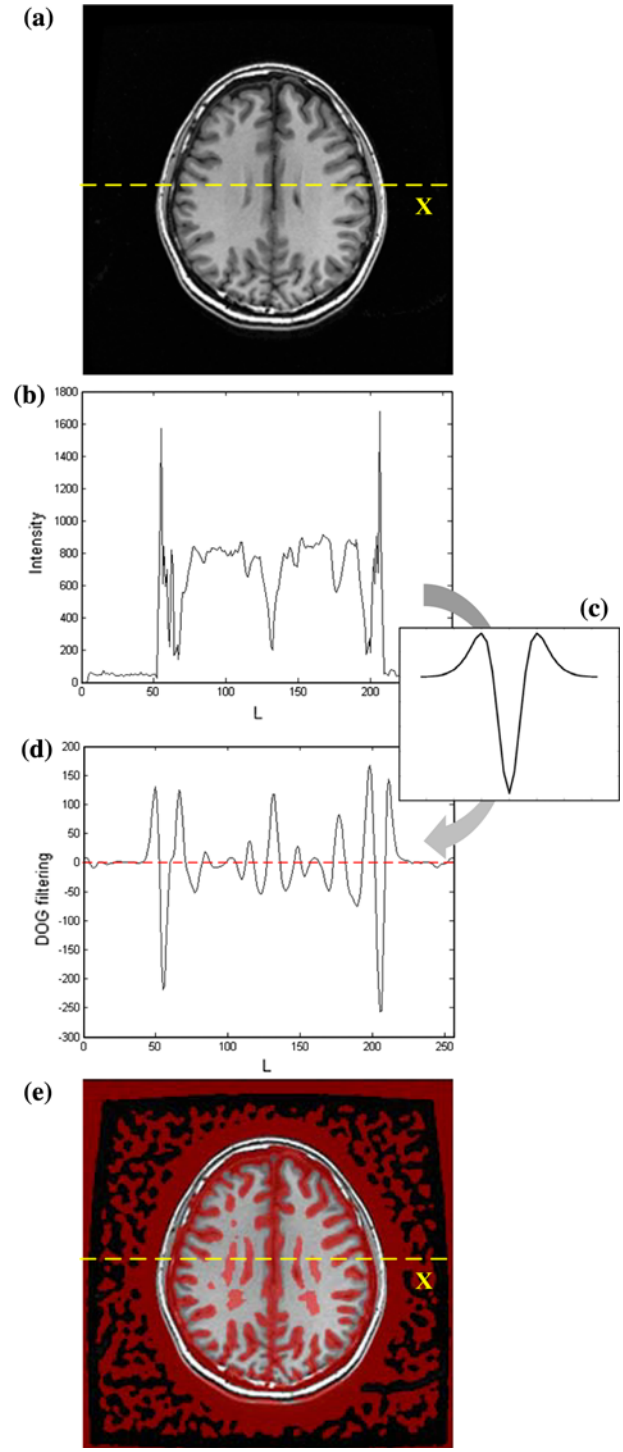

FIGURE 1. The TDOG foreground reveals the regions with relatively low intensities. (a) One axial slice of a T1-weighted MR brain image. (b) The pixel intensity profile on the scan line X. (c) An example of DOG kernel. (d) The results obtained by convolving DOG kernel to the scan line X. (e) Image overlay of the the 2D TDOG foreground (in red color) on the axial slice.

Affine Registration

Overview of the Affine Registration Method

The proposed affine registration method comprises four major steps, as shown in Fig. 2, which determine the 12 degrees of freedom of the transformation $\mathbf{T}_g(\mathbf{p}) = \mathbf{A}\mathbf{p} + \mathbf{b}$, where $\mathbf{b}$ is a translation vector and $\mathbf{A}$ is the transformation matrix representing the rotation, scaling, and shearing of an image volume. Among the 12 parameters of affine registration, the rigid parameters for rotation and translation are highly coupled and hence the estimation accuracy is critical to the whole affine registration process.[39] We estimate the six parameters of the rigid-body transformation by locating the MSPs followed by aligning

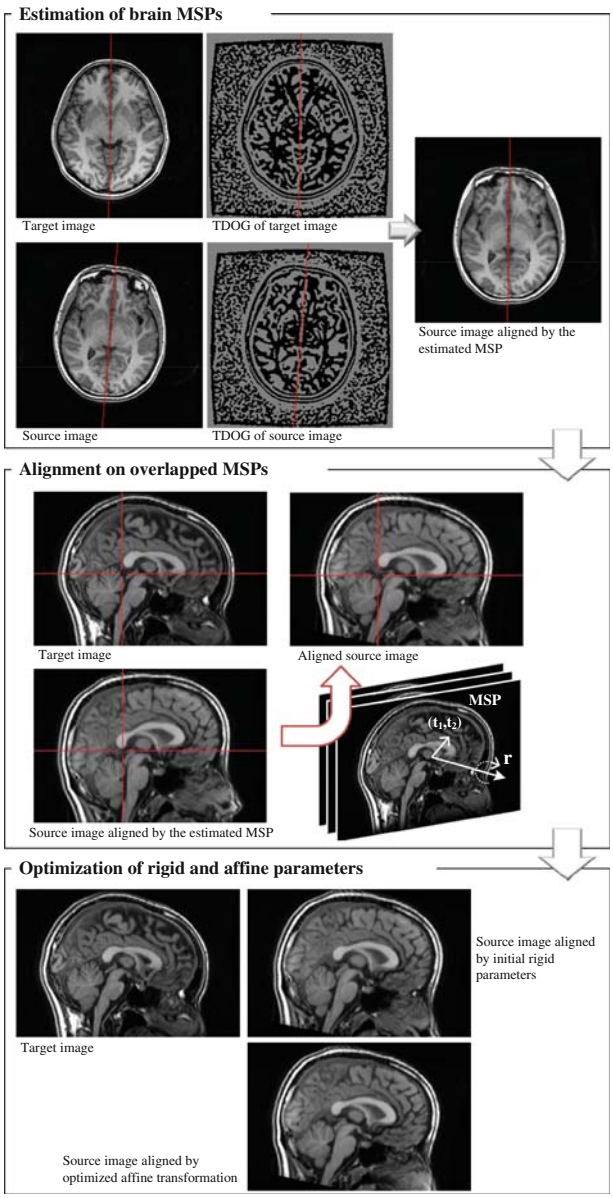

FIGURE 2. Flowchart of the proposed affine registration method. The brain MSPs in the source and target images are determined according to the TDOG images and are then overlapped together. The alignment on the overlapped MSPs is achieved by maximizing the image similarity. The obtained rigid parameters are further refined and then applied to initialize the affine registration of brain images.

brain volumes on the overlapped MSPs, as described in sections "Determination of Brain MSP" and "Alignment on the Overlapped MSPs". Subsequently, the six rigid parameters are further refined and the results provide a good set of initial values in the parameter estimation for affine transformation. The engaged optimization process for the refinement of rigid transformation $\mathbf{T}_r$ and affine transformation $\mathbf{T}_g$ utilizes a hierarchical image structure and the Nelder–Mead downhill simplex method[58] to maximize the correlation ratio (CR), S_{CR} (I_t, I_s, $\mathbf{T}_r$) and S_{CR} (I_t, I_s, $\mathbf{T}_g$), between the spatially mapped source image I_s and target image I_t. Figure 3d shows an example of the alignment results using our affine registration method. Detailed description about CR criterion will be given in section Correlation Ratio.

Determination of Brain MSP

The MSP of a brain is defined as the plane which best separates the two hemispheres.[73] Locating brain MSPs requires the estimation of two rotation and one translation parameters among the six parameters of rigid transform. Some methods of automatic determination of MSPs can be found in references.[4,49,73] In this work, we first estimate the MSP in an analytical way. By utilizing the first order image moment as the work of Smith,[68] the brain centroid is calculated as a point on the initial MSP. The normal vector of the initial MSP is estimated by applying principal component analysis (PCA) to the TDOG image. As the example shown in Fig. 4a, the TDOG foreground is planarly distributed nearby the MSP, whereas the distribution is more isotropic in other regions. Applying PCA to the TDOG image, the two eigenvectors corresponding to the largest two eigenvalues roughly span the MSP and the eigenvector corresponding to the smallest eigenvalue provides an estimate for the normal vector of the MSP. Figure 4b shows that the closed-form solution provides a good initial estimation of the MSP. This initial estimation is further refined toward the "relatively darkest" plane in the brain by maximizing the number of TDOG foreground voxels. This optimization process can improve the MSP determination, as shown in Fig. 4c, as well as the overlapping of the MSPs in the source and target images, which is required in the proposed affine registration method, as shown in Fig. 3b.

Alignment on the Overlapped MSPs

We align the brain volumes on the overlapped MSPs to estimate other three rigid parameters, including a translation vector on the MSP and a rotation angle around the MSP normal. The rotation angle is first estimated by the directions of corpus callosums (CC) segmented from the MSPs. Applying PCA to the segmented CC, the eigenvector corresponding to the largest eigenvalue provides an estimate of the CC direction. Directional difference between CCs gives a good initial estimate of the rotation around the MSP normal. The rotation angle and the translation vector compose a rigid transform $\mathbf{T}_r'$ and are refined by optimizing the CR, $S_{CR}(I_t, I_s, \mathbf{T}_r')$, between the source image I_s and target image I_t. As shown in Fig. 3c, the

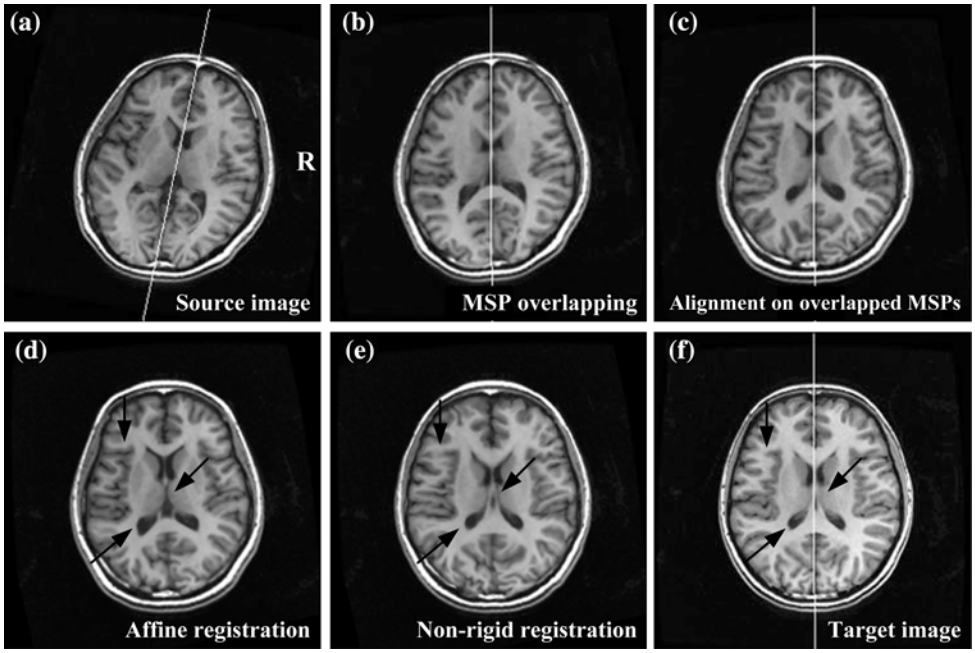

FIGURE 3. Registration between the source image (a) and the target image (f) by using the proposed BIRT methods. The slices shown from (b) to (e) illustrate the results of the MSP overlapping, alignment on the overlapped MSP, affine registration, and non-rigid registration, respectively. The white line in (a) indicates the estimated MSP of the source image whereas those in (b), (c), and (f) indicate the estimated MSP of the target image. The *arrows* in (d) and (e) indicate those areas with stepwise improved alignment refined by the proposed affine and non-rigid methods.

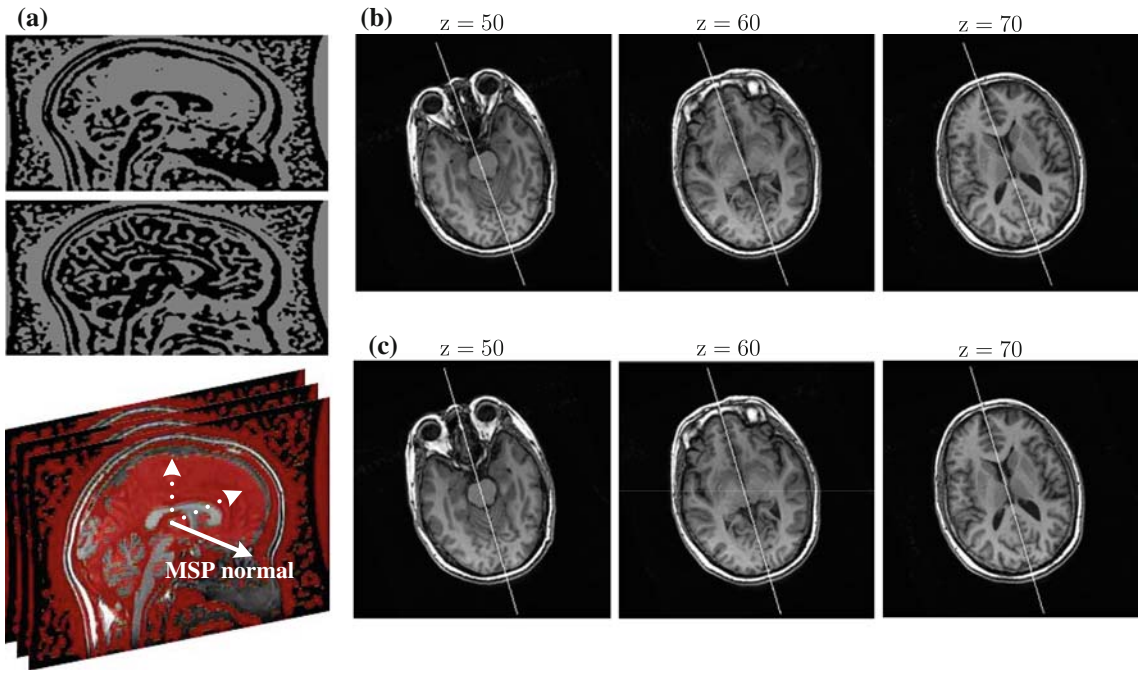

FIGURE 4. Brain MSP estimation and refinement. (a) TDOG image is more planarly distributed nearby the MSP (top), compared to other regions (middle). Applying PCA to the TDOG image, the eigenvector corresponding to the smallest eigenvalue gives an estimate to the MSP normal (bottom). (b) The MSP estimated with an analytical solution. (c) The MSP refined by maximizing the number of foreground TDOG voxels.

proposed method can robustly register brain images, even if there are large rotational differences in some unusual cases.

The segmentation of CC is based on the phenomenon that the intensities of CC in a T1-weighted MR image are significantly larger than those of the

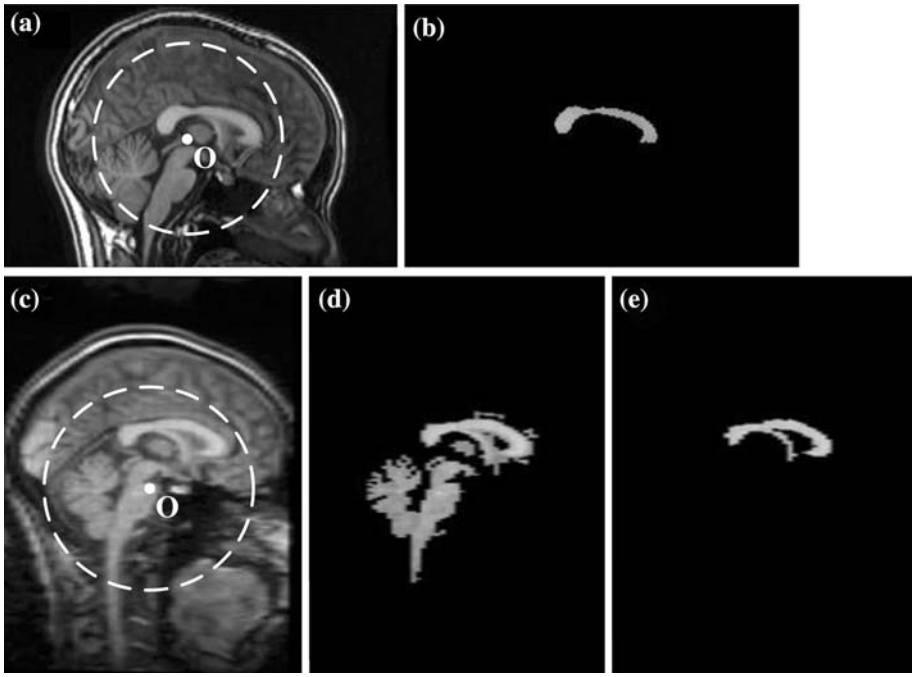

FIGURE 5. Segmentation of CC on MSP. (a) The circular area centered at the gravity of brain MSP, O, is considered in the segmentation of CC. (b) Only one connected region, the CC on MSP, is found in the first thresholding step locates the CC. (c) Excess non-brain tissues can bias the estimation of the circular area considered in the CC segmentation. (d) The intensity differences between CC and the surrounding tissues are not significant and thus many connected regions, the candidates of CC, are found in the first thresholding step. (e) Applying Otsu's method,[54] the calculated intensity threshold can distinguish the CC from other tissues.

surrounding tissues. One or two intensity thresholding steps are used to segment the CC. For each located MSP, we first calculate an effective intensity range $[t_1, t_2]$ to ignore the pixels with unusual intensities, the brain centroid **O**, and a radius r mm which estimates the brain size, as the work of Smith.[68] The segmentation of CC only considers the area within the circle with center at **O** and with radius kr mm, where the value of k is set to be 0.7 in our implementation, as shown in Fig. 5a. All the connected regions with intensity larger than $t_1 + \beta(t_2 - t_1)$ and with area larger than γ are extracted from MSP, where the values of β and γ were set to be 0.7 and 100 mm^2 in BIRT, respectively. We regard the extracted region(s) as the candidate(s) of CC. The segmentation of CC is achieved if there is only one CC candidate, as shown in Fig. 5b. However, the intensity differences between CC and the surrounding tissues can vary considerably and thus the regions other than CC often survive in the first thresholding process, as shown in Fig. 5d. To further distinguish these tissues, we apply Otsu's method[54] to calculate another intensity threshold if there are many CC candidates. Notice that only the pixels in the candidate regions are involved in the calculation. The proposed method can well segment the CC on MSP, even if there are excess non-brain tissues, such as the neck and shoulder areas, as shown in Fig. 5e. Nevertheless, extracting the brain regions beforehand increases the robustness of our segmentation method because it avoids the disturbance of non-brain tissues, which can result in the estimation bias of the brain centroid, as shown in Fig. 5c.

Non-rigid Registration

Non-rigid spatial mapping between brain images is related by a set of Wendland's RBFs with different levels of support extents. Figure 6 shows the flowchart of the proposed non-rigid registration procedure. Non-brain structures are first removed because the inter-subject variation of these regions is relatively large compared to that of brain tissues and hence could interfere with registration efficacy.[80] Therefore, we use a brain mask to extract the brain area as well as the boundary of the brain in the TDOG image, referred as the brain-only TDOG. Though the structures revealed in the brain-only TDOG are quite rough, they provide a guidance to deploy RBFs near the brain boundary, the boundary between GM and WM, and the boundary between CSF and GM/WM. Furthermore, the deformation field is progressively estimated by optimizing the coefficients of each RBF in a coarse-to-fine manner.

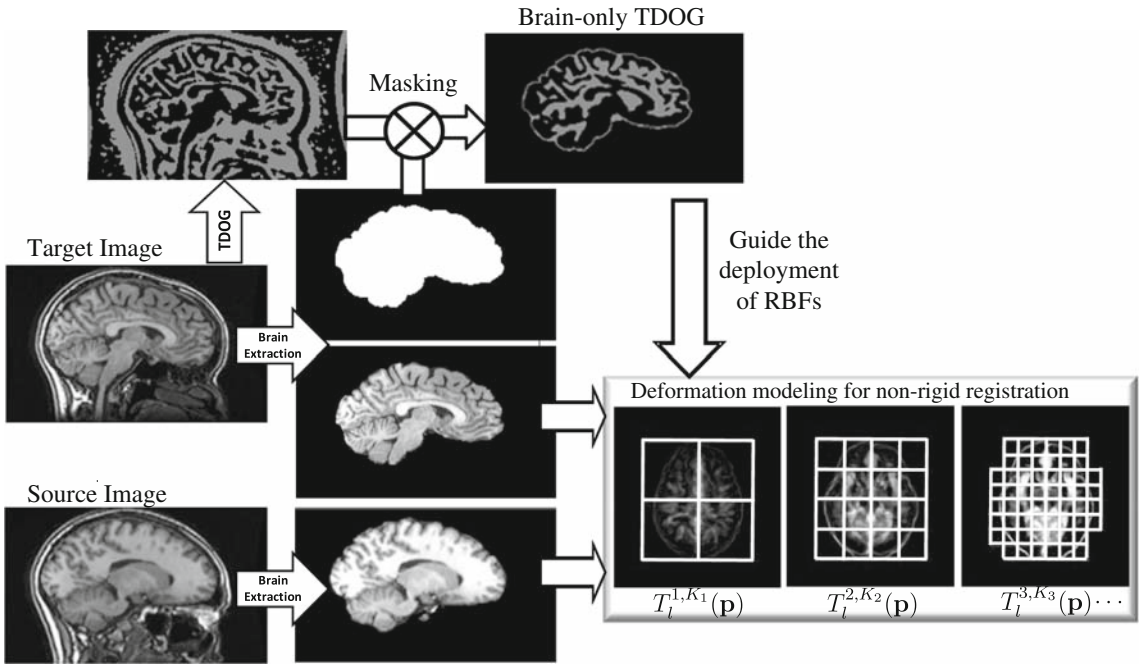

FIGURE 6. Flowchart of the proposed non-rigid registration method. Non-brain regions of the target brain are first removed to obtain a brain mask, which is then used to extract the brain region in the TDOG image of the target brain and construct the brain-only TDOG. The deformation field is modeled by a set of Wendland's RBFs hierarchically distributed at the anatomical structures revealed in the brain-only TDOG.

Non-rigid Transformation Model

We use a combination of K RBFs to model the non-rigid deformation field, $\mathbf{T}_l(\cdot)$,

$$\mathbf{T}_l(\mathbf{p}) = \sum_{i=1}^{K} \alpha_i \phi(\|\mathbf{p} - \mathbf{c}_i\|), \tag{3}$$

where $\|\cdot\|$ is the Euclidean norm and the one-argument function $\phi:\Re_+ \to \Re$ is the RBF centered at $\mathbf{c}_i$ with coefficients $\alpha_i \in \Re^3$, $i = 1, ..., K$. There are different types of RBFs. In this work, we use one of the Wendland's ψ-functions, $\psi_{3,1}$, as the RBF ϕ due to its low computational complexity and the compact support property.[31,78] This function ϕ is formulated as

$$\phi(r) = \begin{cases} (1-r)^4(4r+1), & 0 \le r < 1 \\ 0, & 1 \le r \end{cases}. \tag{4}$$

Based on this set of K RBFs, the positions $\mathbf{c}_i$ and the coefficients α_i, $i = 1, ..., K$, of the RBFs determine the 3-D displacement vector $\mathbf{T}_l(\mathbf{p})$ for each point $\mathbf{p}$ in the image volume.

With the compact support property, the influence of each RBF is restricted to a local region which is a unit sphere around the RBF center. It is a preferred characteristic in non-rigid registration because the deformation of one area should not affect remote regions. This property also greatly alleviates the computational complexity of spatial transformation in contrast to the functions with global support, such as TPS and multiquadrics, because only a few RBFs are involved in the calculation of displacement vector for an image point. To accommodate various extents of compact support, the argument r of the function $\phi(\cdot)$ is scaled by the shape parameter, s.[43] The Wendland's RBF with support extent s is formulated as

$$\phi_s(r) = \phi\left(\frac{r}{s}\right). \tag{5}$$

Hierarchical Decomposition of Deformation Field

For the K RBFs involved in our non-rigid deformation model, there are L different support extents, s_j, $j = 1, ..., L$, each with K_j RBFs and $K_1 + K_2 + ... + K_L = K$. Therefore, the non-rigid deformation field, $\mathbf{T}_l(\cdot)$, can be rewritten as

$$\mathbf{T}_l(\mathbf{p}) = \sum_{j=1}^{L} \sum_{i=1}^{K_j} \alpha_{j,i} \phi_{s_j}(\|\mathbf{p} - \mathbf{c}_{j,i}\|), \tag{6}$$

where $\phi_{s_j}(\cdot)$ denotes the RBF with support extent s_j and coefficients $\alpha_{j,i}$ centered at $\mathbf{c}_{j,i}$. For proper deployment of RBFs, brain volume is hierarchically divided into eight equal subregions, which are cubes in our implementation, and each subregion has an RBF

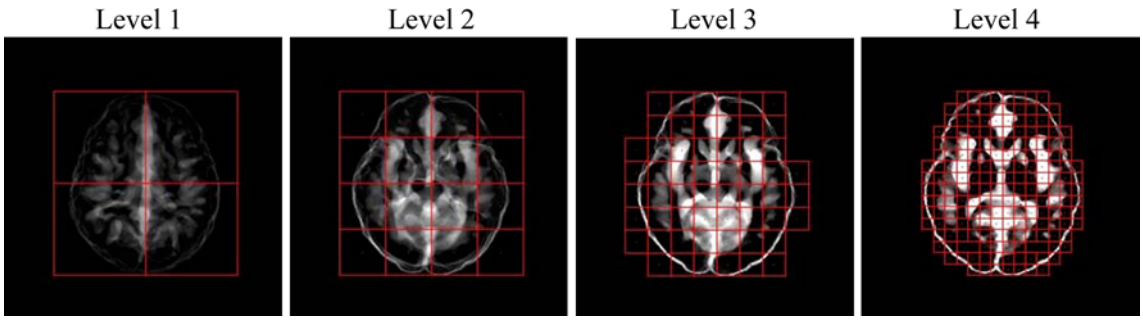

FIGURE 7. The whole brain volume is hierarchically divided into eight subregions. An RBF is deployed at the center of a subregion containing salient structure revealed by the brain-only TDOG. This figure illustrates the RBF distributions at four levels, in which a red square represents a subregion deployed with an RBF.

placed at the center if this region contains any foreground voxels in the brain-only TDOG, as shown in Fig. 7. Although the maximum number of RBFs required at level j is 8^j, the use of brain-only TDOG can help to place necessary RBFs near important anatomical features and avoid the dramatic increase of the number of RBFs. This deployment method is fairly beneficial for computational efficiency while maintaining high registration accuracy, particularly at the fine levels. The support extent s_j at each level j is a parameter which is set to be multiples of the width of subregions. Therefore, the RBFs from low to high levels are capable of modeling the deformation field from coarse to fine resolutions.

Since the deformation field model is hierarchically decomposed into RBFs with different levels of support extent, we estimate the coefficients of RBFs one-by-one while gradually accumulating the deformation field in a coarse-to-fine manner. Consider the coefficient estimation for the m-th RBF at level l. The centered positions and coefficients of the RBFs at the coarser levels from 1 to $l-1$ and the RBFs from 1 to $m-1$ at level l are all determined previously. We update the deformation field by adding a new RBF $\phi_{s_l}(\|\mathbf{p}-\mathbf{c}_{l,m}\|)$ centered at $\mathbf{c}_{l,m}$ with coefficients $\alpha_{l,m}$:

$$\begin{aligned}\mathbf{T}_1^{l,m}(\mathbf{p}) = &\sum_{j=1}^{l-1}\sum_{i=1}^{K_j}\alpha_{j,i}\phi_{s_j}(\|\mathbf{p}-\mathbf{c}_{j,i}\|)\\ &+\sum_{i=1}^{m-1}\alpha_{l,i}\phi_{s_l}(\|\mathbf{p}-\mathbf{c}_{l,i}\|)\\ &+\alpha_{l,m}\phi_{s_l}(\|\mathbf{p}-\mathbf{c}_{l,m}\|).\end{aligned} \tag{7}$$

In this way, the displacement vector for the point $\mathbf{p}$ is progressively updated. The accumulation process terminates when $l=L$ and $m=K_L$, that is, $\mathbf{T}_1(\mathbf{p})=\mathbf{T}_1^{L,K_L}(\mathbf{p})$. Because only three coefficients of an RBF are estimated at a time, the proposed method avoids the searching in a huge parameter space and thus the whole optimization process is quite fast.

Objective Function

Coefficient estimation for each RBF is an optimization process that minimizes an objective function:

$$C(I_t, I_s, \mathbf{T}) = -S_{CR}(I_t, I_s, \mathbf{T}) + \lambda E(\mathbf{T}), \tag{8}$$

where $\mathbf{T}$ is the spatial mapping between the target image I_t and the source image I_s, S_{CR} measures the image similarity by CR, the smoothness regularization function E calculates the deformation energy of $\mathbf{T}$, and the parameter λ compromises the measurements S_{CR} and E. The Laplacian model and the thin-plate model are widely applied to regularize the structure deformation in image registration.[62] Due to the computational efficiency, we adopt the Laplacian model in this work:

$$E(\mathbf{T}) = \frac{1}{V}\iiint\left[\left(\frac{\partial\mathbf{T}}{\partial x}\right)^2+\left(\frac{\partial\mathbf{T}}{\partial y}\right)^2+\left(\frac{\partial\mathbf{T}}{\partial z}\right)^2\right]dxdydz, \tag{9}$$

where V is the volume involved in the estimation. The Nelder–Mead downhill simplex method is utilized to optimize the objective function. Figure 3e demonstrates that the proposed non-rigid method can well register the corresponding anatomical structures.

Implementation Issues

In the optimization process of non-rigid registration, iterative calculation of image transformation contributes to the major computation burden, particularly when registering high resolution image volumes. The hierarchical decomposition of the non-rigid transformation model and the compact support property of Wendland's RBFs are both beneficial to the alleviation of this heavy burden. However, the execution time of non-rigid registration is still large. Some implementation techniques described below are helpful to further improve the efficiency. First, we construct a volume pyramid with L' levels for each MR image

volume, generally $L' \leq L$. When evaluating the objective function, the K_j RBFs, $\phi_{s_j}(\cdot)$ with support extent s_j, $j = 1, ..., L$, are associated with the j'-th level of volume pyramid, where $j' = j$ when $j \leq L'$ and $j' = L'$ when $j > L'$. This hierarchical architecture enables a coarse-to-fine optimization that helps to avoid the local traps and improves the computational efficiency. Second, one lookup table is constructed beforehand for each support extent level of Wendland's RBFs to avoid the repeated function evaluations. Therefore, updating the deformation field with the RBF $\phi_{s_j}(\cdot)$ in Eq. (7) requires only three subtractions, one table lookup, three multiplications, and three additions.

Correlation Ratio

The image similarity function has strong influence on registration results. Statistical measurements such as MI,[23,76] NMI,[69] and CR[60] have been used in multimodal image registration.[33,57,83] These measurements are also adequate to unimodal image registration because they are robust to the noise, the different intensity contrast, and the intensity inhomogeneity. In this work, CR is adopted because it is superior in accuracy, efficiency, and robustness.[39,56,60]

For the voxels of the same tissue in the target image, CR measures the intensity dispersion for their corresponding points in the source image. Let N be the number of voxels in the overlapping region Ω between the source image I_s and the target image I_t. We divide the whole intensity range into N_B bins: B_i, $i = 1, ..., N_B$. Let X_i denote a set of voxels in the region Ω of the source image satisfying that their corresponding voxels in the target image have intensities belonging to the same intensity bin, B_i, as shown in Fig. 8. That is,

$$X_i = \{\mathbf{p} \mid \mathbf{p} \in \Omega, I_t(\mathbf{F}(\mathbf{p})) \in B_i\}, \tag{10}$$

where $\mathbf{F}$ can be the spatial transformation function $\mathbf{T}_r$, $\mathbf{T}_r'$, $\mathbf{T}_g$, or $\mathbf{T}$ in this work. Notice that $N_1 + N_2 + \cdots + N_{N_B} = N$, where N_i is the number of voxels in X_i. Image similarity based on CR is calculated by

$$S_{CR}(I_t, I_s, \mathbf{F}) = 1 - \frac{1}{\mathrm{Var}(I_s(\Omega))} \sum_{i=1}^{N_B} \frac{N_i}{N} \mathrm{Var}(I_s(X_i)), \tag{11}$$

where function $\mathrm{Var}(I_s(\Omega))$ and $\mathrm{Var}(I_s(X_i))$ evaluate the intensity variances of source image in Ω and X_i, respectively. The voxels belonging to the same tissue generally have similar intensities. In the target image,

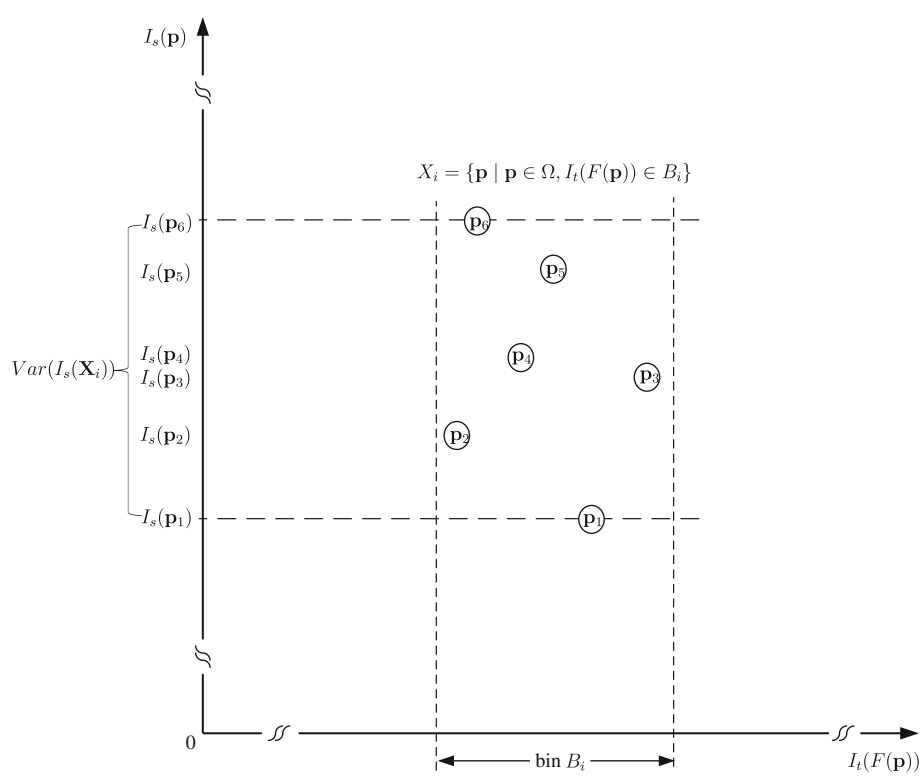

FIGURE 8. CR measures the intensity dispersion for the voxel set X_i in the source image which contains voxels with their corresponding points in the target image belonging to the same intensity bin B_i.

therefore, the voxels having intensities within each intensity bin B_i very likely belong to the same tissue. If the source and target images are well aligned, voxels in X_i of the source image should also belong to the same tissue and hence the intensity variance of X_i should be small. Consequently, larger CR value indicates higher image similarity and hence better alignment.

Evaluation of Registration Performance

This section introduces the methods used to evaluate the performance of the proposed affine and non-rigid registration algorithms, including the data sets and the approaches used for comparisons.

Registration Algorithms for Performance Comparisons

The proposed affine registration method in BIRT was compared with Statistical Parametric Mapping 2 (SPM2),[10] Automated Image Registration version 5.2.5 (AIR5),[79] and FMRIB's Linear Image Registration Tool version 5.5 (FLIRT).[39] The proposed non-rigid registration method in BIRT was compared with SPM2,[7] Hierarchical Attribute Matching Mechanism for Elastic Registration version 1.0 (HAMMER),[66] and Diffeomorphic Anatomical Registration Through Exponentiated Lie algebra (DARTEL)[5] in SPM5. BIRT was implemented in C++ and the programs of other algorithms were downloaded from their webpages. All registration experiments were executed on a PC with an AMD Opteron 1.4 GHz processor running Linux.

Data Sets with Known Spatial Mapping Relation

T1-weighted head MR images acquired on a 1.5 Tesla GE MR scanner (3D-FSPGR pulse sequence; TR = 8.67 ms, TE = 1.86 ms, TI = 400 ms, NEX = 1, flip angle = 15°, bandwidth = 15.63 kHz) were used to construct simulation data in our experiments. Both the experiments of affine and non-rigid registration quantitatively measured the alignment accuracy and execution efficiency using two sets of images, each set with 30 images, with different spatial resolutions ($256 \times 256 \times 124$, voxel size = $1.02 \times 1.02 \times 1.5$ mm^3 and $128 \times 128 \times 34$, voxel size = $2 \times 2 \times 5$ mm^3). The registration error was evaluated by the average deviation of the estimated displacement vectors from the ground-truth ones, and the computational efficiency was compared according to the average execution time for registering an image pair.

Both the low- and high-resolution data sets applied in the experiment of affine registration were constructed by applying 30 times of affine transformation to each of the 30 MR images originally scanned, each time with random transformation parameters uniformly distributed within $[-\pi/15, \pi/15]$ in radian, [−15 mm, 15 mm], [−0.05, 0.05], and [−0.01, 0.01] for rotation, translation, scaling, and shearing, respectively. In the accuracy evaluation, each originally scanned MR image was regarded as the source image and the randomly transformed images were regarded as the target images, one at a time. The known random transformations provided the ground truths of corresponding points. Moreover, the rigid parameters of the ground truths with the same image set were also used to evaluate the accuracy of the rigid transformation estimated by the proposed method.

Three sets of source–target pairs of brain images, low and high resolution, with known deformation fields were constructed by applying SPM2, HAMMER, and DARTEL to nonlinearly register 30 originally scanned MR images to a specified target image. We regarded the originally scanned images, the deformed images, and the deformation fields obtained by each registration method as the source images, the target images, and the ground truths of deformation, respectively, to evaluate the performance of other three algorithms. These materials facilitate the performance evaluation in a more objective way because the results are not biased toward a specific deformation type. The value to threshold the TDOG image can affect the performance of our non-rigid registration method, in terms of alignment accuracy and computational efficiency. Therefore, the constructed image pairs were also used to evaluate the influences of the thresholding level.

Parameters of Registration Algorithms

In our experiments, the parameters of the compared methods were set to their default values, except AIR5. The intensity thresholds in AIR5 were set to the values which can exclude most of the background voxels and the scales of Gaussian kernels were determined by the best average accuracy. Two necessary preprocesses in HAMMER, brain extraction and tissue segmentation, were accomplished by Brain Extraction Tool version 2.1 (BET2)[68] and FMRIB's Automated Segmentation Tool version 4.1,[82] which are parts of the FMRIB's Software Library.[67] For our affine and non-rigid methods, we set the FWHM of the Gaussian variances (σ_1^2, σ_2^2) in TDOG to be (4 mm, 3 mm). The proposed non-rigid method applied BET2 to obtain brain masks and the RBF support extent was set to be 1.5 times of the subregion width.

Effects of Registration Accuracy on VBM Analysis

This section introduces the experiment designed to investigate the influence of registration accuracy on the

results of VBM analysis, including the construction of image groups and the criteria used for quantitative evaluation.

Construction of Image Groups

Six groups of GM images were generated by applying TPS transformation to deform a phantom GM image obtained from BrainWeb.[25] This avoids the segmentation step in VBM protocol[8,34] such that the analysis results were not confounded by segmentation error. One normal group and five patient groups with different scales of volume differences were generated in this experiment, in which each group contained 30 subjects and all the images were 157 × 189 × 156 with voxel size 1.0 mm^3. Some related techniques for generating brain images with volumetric changes can be found in references.[19,20,40]

A total of 208 control points on the cortical surface of the cerebrum and cerebellum were selected to create MR brain images with or without volume difference in the cerebellum. Thirty of these points, referred as

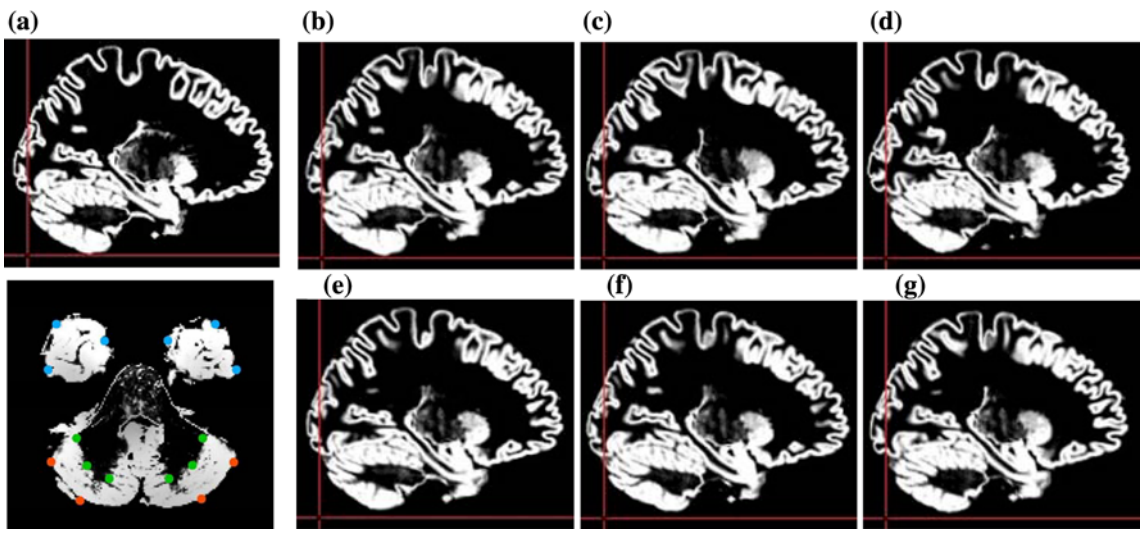

FIGURE 9. The construction of simulated images with different degrees of volume difference in the cerebellum. (a) All the images were constructed from the BrainWeb phantom GM (top) by using the TPS transformation. An inferior slice (bottom) of the phantom image illustrates the distribution of the control points. The red points placed on the exterior cortical surface of the cerebellum are used to generate volume difference patterns in the cerebellum. The green and the blue points distributed on the interior cortical surface of cerebellum and the cortical surface of cerebrum, respectively, are used to fix anatomical structures. The following figures illustrated the constructed MR images with different scales of volume differences: (b) 0 mm (normal subject), (c) 2 mm, (d) 3 mm, (e) 4 mm, (f) 5 mm, and (g) 6 mm.

TABLE 1. Performance comparison of affine registration algorithms.

		BIRT									
					Affine						
Performance criteria	MDM	MSP overlap	MSP alignment	Rigid	Level 1	Level 2	Level 3	Level 4	FLIRT	SPM2	AIR5
Error (mm)^H	22.83	9.79 (9.09)	3.34 (1.62)	3.30 (1.46)	2.98	0.78	0.20	0.05	0.28	0.57	3.52
Time (sec)^H	–	27 (26.89)	45	51	51	53	76	364	442	51	131
Error (mm)^L	22.80	9.89 (9.83)	7.80 (3.35)	3.35 (2.62)	3.00	0.76	0.21	0.06	0.37	0.94	4.00
Time (sec)^L	–	1 (0.99)	9	12	12	13	28	43	120	21	7

The upper and lower parts list the results of experiments using images with higher and lower spatial resolution, respectively. The first column lists the mean displacement magnitude (MDM) calculated from the spatial mapping relation of image pairs. The following seven columns list the averaged performance of the proposed BIRT method step-by-step, including the MSP overlapping, the alignment on the overlapped MSP, the rigid registration, and the affine registration across four multi-resolution levels. To demonstrate the accuracy of rigid transformation estimation, the numbers shown in the parentheses of the Error rows are the average alignment error when only the rigid parameters of the ground truths are considered. The average execution times used to calculate the TDOG images are listed in the parentheses of the Time rows. Note that the execution time of BIRT is accumulated for each step. The last three columns list the performance indices for FLIRT, SPM2, and AIR5.

^{H}256 × 256 × 124 images with voxel size 1.02 × 1.02 × 1.5 mm^3.

^{L}128 × 128 × 34 images with voxel size 2 × 2 × 5 mm^3.

manipulating points, were identified on the exterior cortical surface of the cerebellum and were used to generate difference patterns with different scales. The other 178 points were used to fix anatomical structures, in which 38 points were selected from the interior surface of the cerebellum and 140 points were placed on the surface of the cerebral cortex. Figure 9a illustrates the placement of these control points.

MR brain images of the normal subjects and patients were constructed by the following procedures. There are three steps in the generation of a patient image. First, we moved the manipulating points toward the cerebellum center. The displacement magnitude, that is, the volume difference scale, was parameter-controlled. Second, all the 208 control points were moved by a random vector with uniformly distributed magnitude within 2 mm in order to model the inter-subject structure variation. In the last step, we applied TPS transformation to construct a patient image according to these 208 control points. The construction procedure for a normal subject was the same as that for a patient, except the scale of volume difference was set to zero. In our experiments, the magnitude of the volume difference was uniformly distributed within different scales. Figures 9b–9g show the examples of the constructed images with difference scale of 0 (normal subject), 2, 3, 4, 5, and 6 mm, respectively.

Accuracy Assessment of VBM Analysis

Two non-rigid registration algorithms, SPM2 and BIRT, were applied in the VBM analysis procedure. Normal subjects and patients were first registered to the GM phantom and the obtained deformation fields were used to modulate the deformed images for GM volume estimation.[8] The modulated images were convolved by a Gaussian kernel (FWHM = 4 mm) and the resulted images were statistically analyzed by using two-sample *t*-test.

We examined the VBM analysis procedure and defined proper ground truths for quantitative comparison. VBM structure analysis uses a registration method to normalize all subjects into the same stereotaxic space such that the corresponding structures are aligned and the structure variances between subjects can be removed. Therefore, the MR images

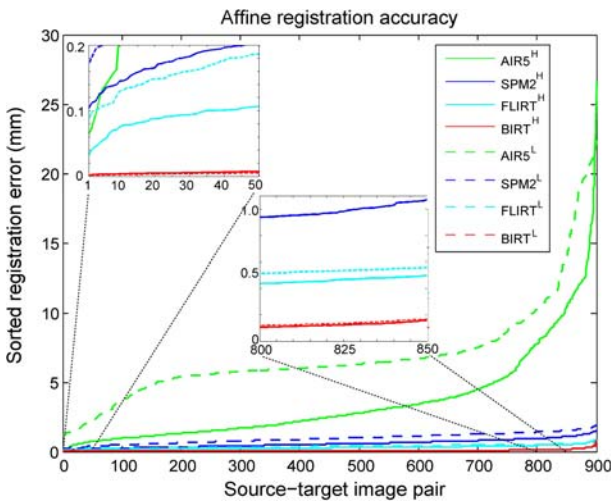

FIGURE 10. Comparison for the stability and accuracy of affine registration algorithms. The solid (dashed) lines show the results of experiments using 256 × 256 × 124 (128 × 128 × 34) images with voxel size 1.02 × 1.02 × 1.5 (2 × 2 × 5) mm^3.

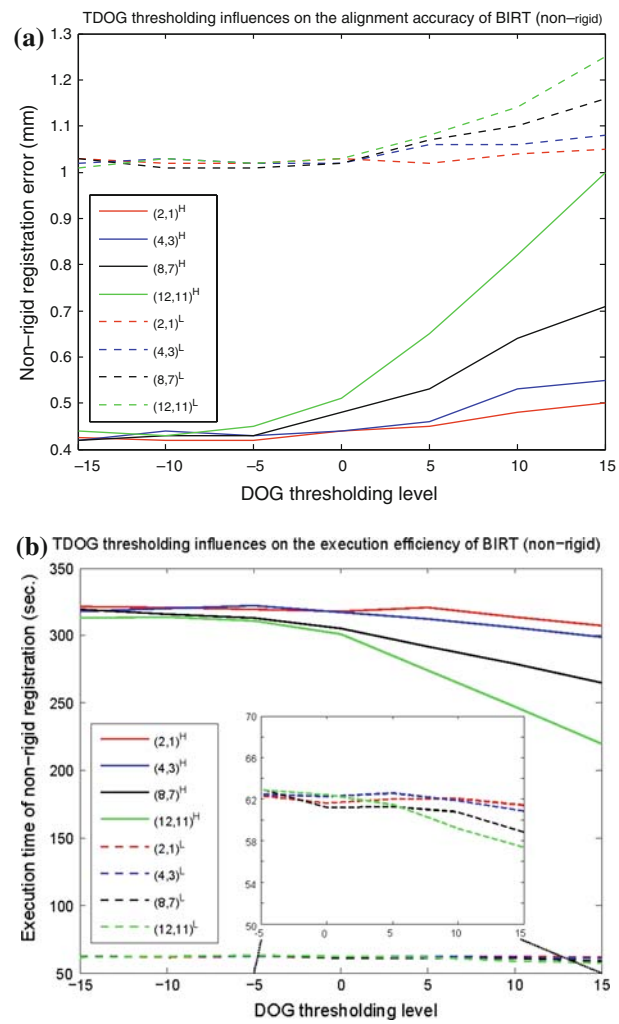

FIGURE 11. Influences of the thresholding value in TDOG upon the alignment accuracy and computational efficiency of our non-rigid registration method. Four different FWHM settings for the Gaussian variances were evaluated, including (12, 11 mm), (8, 7 mm), (4, 3 mm), and (2, 1 mm). The solid (dashed) lines show the results of experiments using 256 × 256 × 124 (128 × 128 × 34) images with voxel size 1.02 × 1.02 × 1.5 (2 × 2 × 5) mm^3. Notice that the listed computational efficiency excluded the execution time of the required brain extraction and affine registration processes.

transformed by a perfect registration method should be identical to the target (the GM phantom in this experiment). According to this viewpoint, the structural discrepancies discovered by the VBM analysis with a perfect registration method were the subtraction between the phantom image (that is, the perfectly registered images of normal subjects) and the phantom image modulated by the TPS deformation field (that is, the perfectly registered patient images). We applied Gaussian kernel (FWHM = 4 mm) to smooth the obtained ground truths of different scales of volume differences because the same kernel was applied to convolve the normalized and modulated subjects before the statistical analysis.

Correlation coefficient provides another quantitative measurement showing that whether accurate registration can facilitate VBM procedure to reveal more accurate statistical inferences. The voxels with higher values in the Gaussian smoothed ground truth indicate that there are larger volume differences between groups. For an accurate VBM analysis, the positions of these voxels in the t-map obtained from VBM results should have higher significance. Therefore, the higher correlation coefficient between the ground truth and the t-map implies that the VBM analysis can reveal regions with volume differences more accurately.

EXPERIMENTAL RESULTS

This section presents our experimental results, including the validation of registration performance and the investigation for the influences of registration accuracy upon VBM analysis.

Comparison of Affine Registration Algorithms

Table 1 lists the performance comparisons for affine registration algorithms in terms of execution time and mean registration error calculated from all image voxels. For BIRT, the performance indices of the estimation for rigid parameters and the affine registration across four multi-resolution levels are listed in the table. The results of our experiment using high- (low-) resolution images showed that BIRT can achieve better accuracy than other algorithms in 76 (28) s, which is longer than that of SPM2 (SPM2 and AIR5) within 30 s. We can observe that the initial rigid transformation estimated by the proposed method is quite accurate, which was 1.46 (2.62) mm in the alignment of high- (low-) resolution images when only the rigid parameters of the ground truths are considered. It is apparent that the alignment error of the subsequent affine registration decreases rapidly from coarse to fine levels. Figure 10 plots the sorted registration accuracy for all methods. The relatively low increasing rate indicates that BIRT can stably register brain image volumes. This figure also shows that the accuracy of about 95% cases was smaller than 0.1 mm by using the proposed method in this experiment. From Table 1 and Fig. 10, we can see that good spatial resolution of images can benefit the alignment accuracy for all compared methods at the expense of longer execution time. Nevertheless, BIRT was less sensitive to image resolution in contrast to other algorithms.

Determination of TDOG threshold

Figure 11 illustrates the performance of our non-rigid method with respect to different settings of the Gaussian variances and TDOG threshold.

TABLE 2. Performance comparison of non-rigid registration algorithms.

		BIRT								
Data set	MDM	Affine	L1	L2	L3	L4	L5	SPM2	HAMMER	DARTEL
SPM2 data^{H}	17.44/–	2.74/113 (47)	2.67/116	1.55/121	0.77/141	0.33/242	0.19/321	–	0.59/8845 (3766)	0.52/12783 (2145)
HAMMER data^{H}	14.39/–	2.67/119 (33)	2.53/125	1.96/150	1.22/278	0.65/350	0.34/415	2.07/276	–	1.92/11480 (1950)
DARTEL data^{H}	14.49/–	2.86/114 (33)	2.02/119	1.86/141	1.60/251	1.12/311	0.78/367	2.26/298	1.01/8646 (3777)	–
SPM2 data^{L}	17.49/–	3.75/45 (8)	3.44/46	2.70/71	1.52/98	0.80/110	0.60/121	–	1.17/781 (135)	2.03/11273 (1011)
HAMMER data^{L}	13.39/–	2.95/43 (8)	2.82/43	2.64/64	2.05/84	1.36/94	1.03/102	2.02/194	–	2.15/11594 (933)
DARTEL data^{L}	15.49/–	2.91/32 (8)	2.16/32	2.04/51	1.94/69	1.70/78	1.45/85	2.42/186	2.23/595 (125)	–

The upper and lower parts show the results of experiments using images with higher and lower spatial resolution, respectively. For each part, the performance indices with the images constructed by SPM2, HAMMER, and DARTEL are listed from top to bottom. The first column lists the mean displacement magnitude (MDM) calculated from the spatial mapping relation of image pairs. The following six columns list the performance of the proposed BIRT method. The last three columns list the registration performance of SPM2, HAMMER, and DARTEL. The numbers before and after the slash are the registration error and the execution time, respectively. The numbers in parentheses show the preprocessing time if required. Note that the execution time of BIRT is accumulated for each step.
mm/s (s).
$^{H}256 \times 256 \times 124$ images with voxel size $1.02 \times 1.02 \times 1.5$ mm^3.
$^{L}128 \times 128 \times 34$ images with voxel size $2 \times 2 \times 5$ mm^3.

Our experimental results showed that a smaller TDOG threshold, which increases the amount of structure information, generally resulted in better alignment accuracy at the expense of longer execution time. We can observe that both the alignment accuracy and computational efficiency of our non-rigid method converged when the threshold was smaller than -5. Gaussian variances also determine the amount of the structure information, coarse or fine. With the same thresholding level, it can be observed that the Gaussian variances providing coarse structure information commonly resulted in efficient registration process at the cost of high alignment error. Our experimental results also showed that the TDOG threshold had greater influences upon the registration performance for high-resolution images compared to that for low-resolution images. Compromising the registration accuracy and execution efficiency, we empirically determined the values of the FWHMs of the Gaussian variances σ_1^2 and σ_2^2 and the TDOG thresholding level to be 4, 3, and 0 mm, respectively.

Comparison of Non-rigid Registration Algorithms

Table 2 shows the evaluation results of BIRT (both the affine and non-rigid methods), SPM2, HAMMER, and DARTEL, in which the registration error was calculated from the voxels in the brain area. Both the experiments using high- and low-resolution images indicated that the registration error of BIRT steadily decreased across five deformation levels and achieved better accuracy than other algorithms in a short period of time. It can be observed that HAMMER, DARTEL, and BIRT performed better for the simulation images constructed by SPM2, compared to other data sets. The registration accuracy of BIRT at the second (third) deformation level was comparable to that of SPM2 with the high- (low-) resolution HAMMER and DARTEL data sets. The registration errors of HAMMER and BIRT for the images constructed by DARTEL were relatively higher than those for other data sets. On the other hand, in the experiments using high-resolution images, DARTEL did not perform as well for the alignments of the HAMMER data set as that of the SPM2 data set. Figure 12 illustrates the sorted accuracy for the experiments of all data sets. From the increasing rate of the profiles, we can see that the registration processes of all non-rigid methods were quite stable, except for SPM2 with the DARTEL data set and HAMMER with the low-resolution DARTEL data set. Our experimental results also indicated that the alignment of high-resolution images can achieve better accuracy at the expense of longer execution time compared to the registration of low-resolution data. Notice

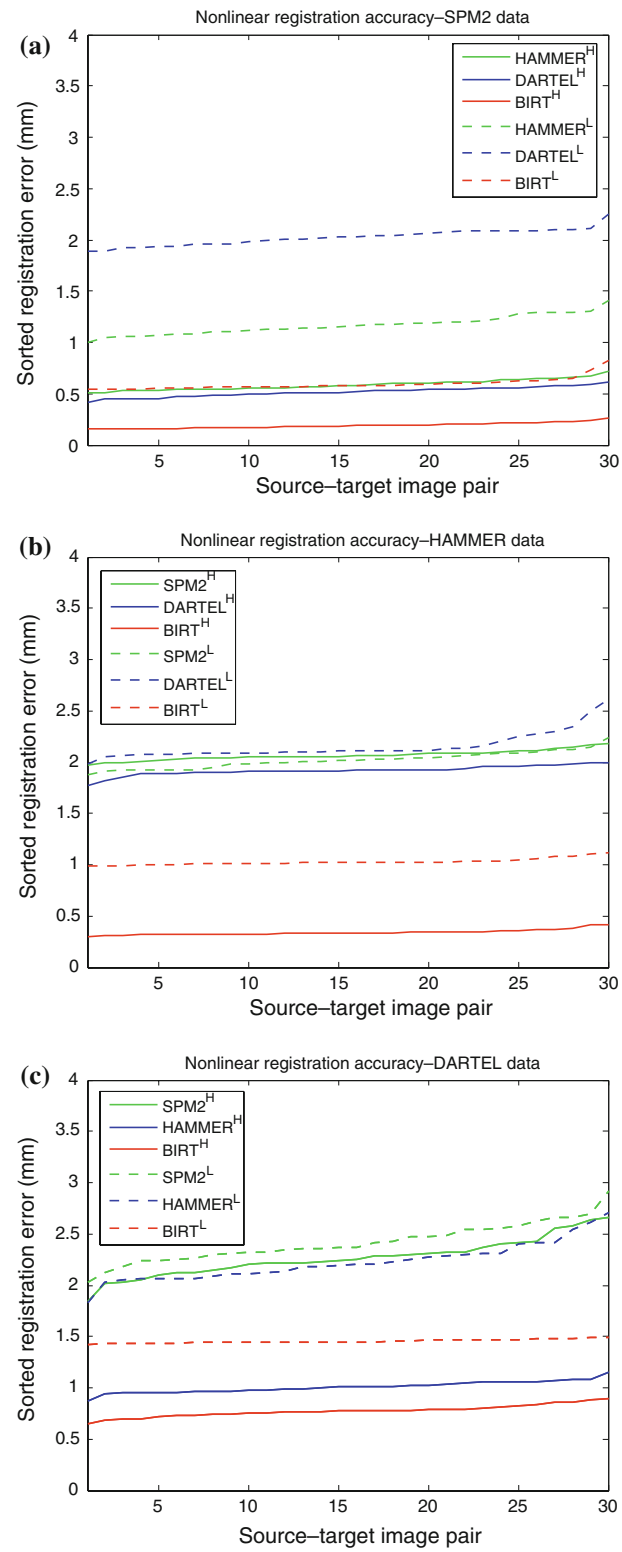

FIGURE 12. Comparison for the stability and accuracy of non-rigid registration algorithms with the simulated images constructed by (a) SPM2, (b) HAMMER, and (c) DARTEL. The solid (dashed) lines show the results of experiments using 256 × 256 × 124 (128 × 128 × 34) images with voxel size 1.02 × 1.02 × 1.5 (2 × 2 × 5) mm^3.

that the execution efficiency of DARTEL did not improve significantly for low-resolution images, possibly because DARTEL imports data with the same spatial resolution, 1.5 mm^3.

Effects of Registration Accuracy on VBM Analysis

Figure 13 shows the results of VBM analyses using two different registration algorithms, SPM2 and BIRT. It can be seen that the revealed patterns of volume difference ($p < 0.005$) using BIRT are more focal in all cases. This figure also depicts that the VBM analysis using SPM2 non-rigid registration presents more false volume differences, particularly in the groups with larger difference scales. Comparing the ground truths with the VBM results of various thresholds for significance level, we obtained the receiver operating characteristics (ROC) of each

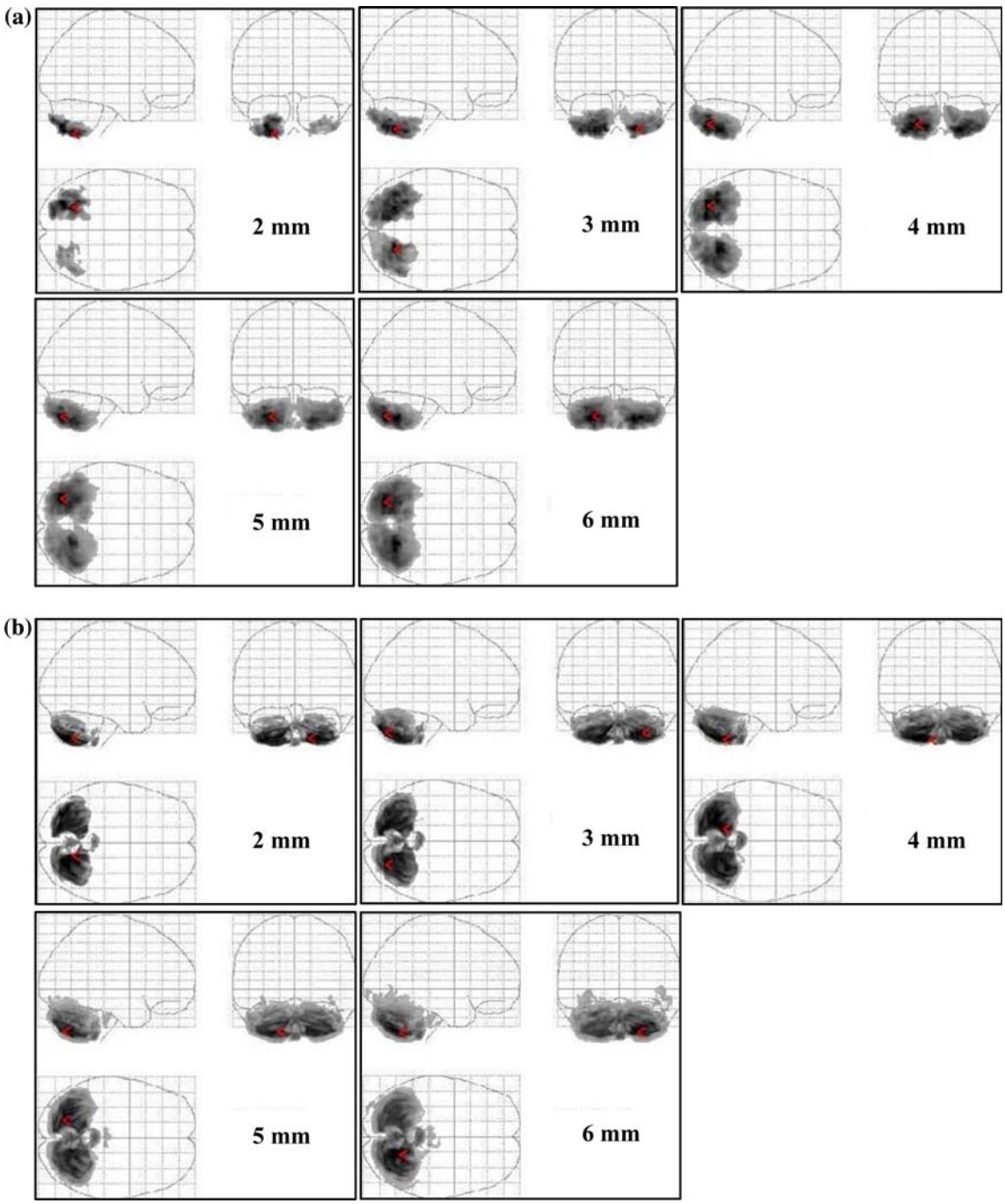

FIGURE 13. The VBM structural analysis results ($p < 0.005$) using simulated images with different scales of volume differences, in which the image normalization was performed by using (a) BIRT and (b) SPM2.

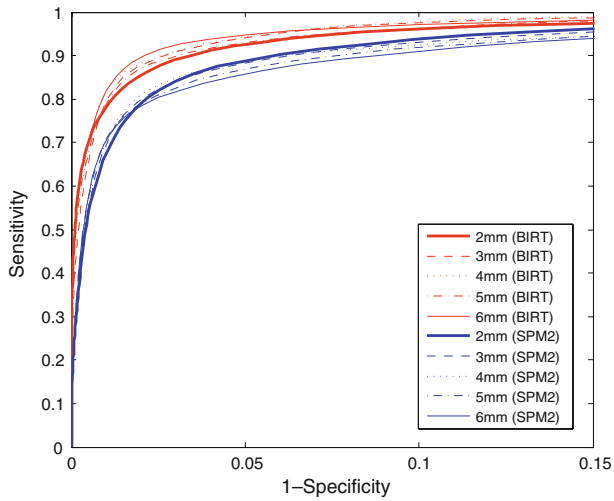

FIGURE 14. The ROC curves of the simulated VBM structural analyses, in which the red and blue curves represent the results with different scales of volume differences from 2 to 6 mm using BIRT and SPM2, respectively.

TABLE 3. The correlation coefficients between the ground truths and the t-maps obtained from VBM analysis using BIRT and SPM2 methods.

	Scale of volume difference				
	2 mm	3 mm	4 mm	5 mm	6 mm
SPM2	0.61	0.61	0.63	0.60	0.58
BIRT	0.65	0.67	0.74	0.74	0.74

registration algorithm. According to the ROC curves shown in Fig. 14, BIRT is superior to SPM2 with respect to sensitivity and specificity. Table 3 lists the correlation coefficients between the ground truths and the t-maps. Apparently, BIRT has higher values and thus is superior to SPM2 in all cases.

DISCUSSION

The proposed affine method registers brain images by optimizing the 12 parameters subsequent to the estimation of the rigid transformation. Generally, rigid parameters are highly coupled and are critical to accurate registration results. Due to the use of structure information, BIRT can robustly estimate the orientation and position differences between MR images of the brains and the estimation error is small in our experiments. Therefore, the rigid transformation can provide a good initial for the optimization of all affine parameters, even if there are large orientation differences, as the example shown in Fig. 15. Both FLIRT and BIRT can find the correct orientation in such cases. However, FLIRT achieves this goal by searching in a large space of parameters at the expense of longer execution time than that of BIRT. Experimental results showed that the proposed affine method performs well in terms of accuracy, efficiency, and stability.

The determination of brain MSP is an essential step in our affine registration algorithm. In general, previously published methods[4,49,73] can be applied to locate

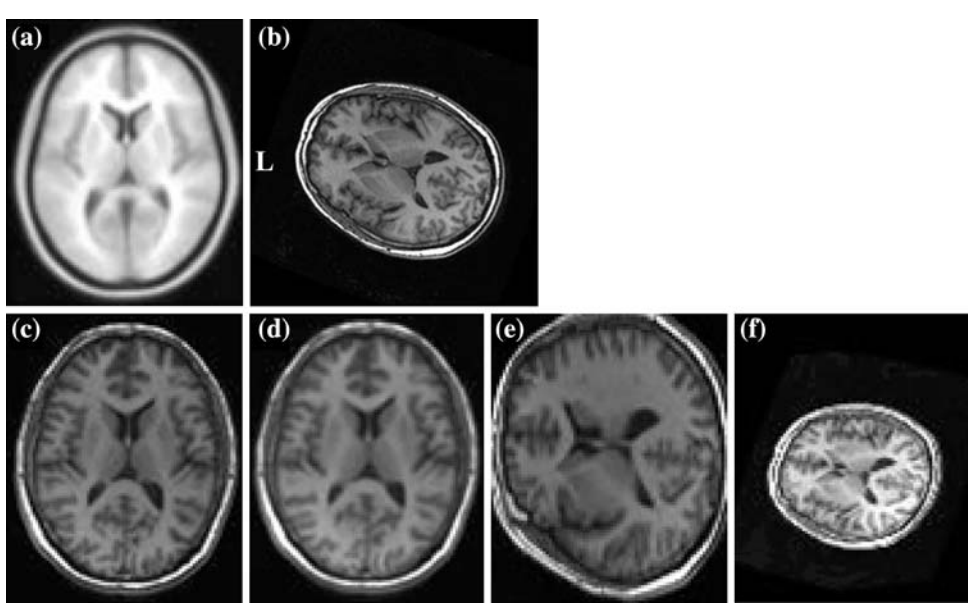

FIGURE 15. The affine registration for brains with large orientation difference. (a) The ICBM-152 brain template used as the target image. (b) A T1-weighted image used as the source image. The affine-registered result using (c) BIRT, (d) FLIRT, (e) SPM2, and (f) AIR5.

the MSP in the proposed procedure. In this work, we propose a new MSP location method based on the TDOG image. Because of the structural properties of MSP revealed in the TDOG image, the orientation of MSP can be estimated by a closed-form solution and the further refinement is very time efficient. As shown in Table 1, the major computational burden of our method is from the Gaussian filtering procedure in the TDOG image computation. Because the TDOG image is necessary for the subsequent non-rigid registration process, the proposed MSP location method only slightly increases the whole computation with the centroid estimation, the PCA computation of 3×3 matrices, and the following optimization procedure. Moreover, the TDOG image and the PCA procedure can reduce the influence of noise and intensity inhomogeneity. Even when the neck and shoulder regions are included in the images and could largely bias the estimation of brain centroid, the MSP can also be robustly located by the proposed affine method, as the example shown in Fig. 16.

Extracting the brain region beforehand is usually beneficial to registration accuracy because the inter-subject variation of non-brain structures are relatively large.[80] Nevertheless, brain extraction is not included as a necessary step in the proposed affine method for the generality of methodology. Notice that the estimation to brain orientation in the proposed affine method is only adequate to the registration of brain images because it uses the information specific to brain structures. Therefore, it is not a solution to general rigid registration problems.

A non-rigid registration method in BIRT applies Wendland's RBFs to model image deformation field hierarchically, in which all RBFs are adaptively deployed near the important structures of brains. Execution efficiency is an important issue for the alignment of 3-D images, especially for those applications

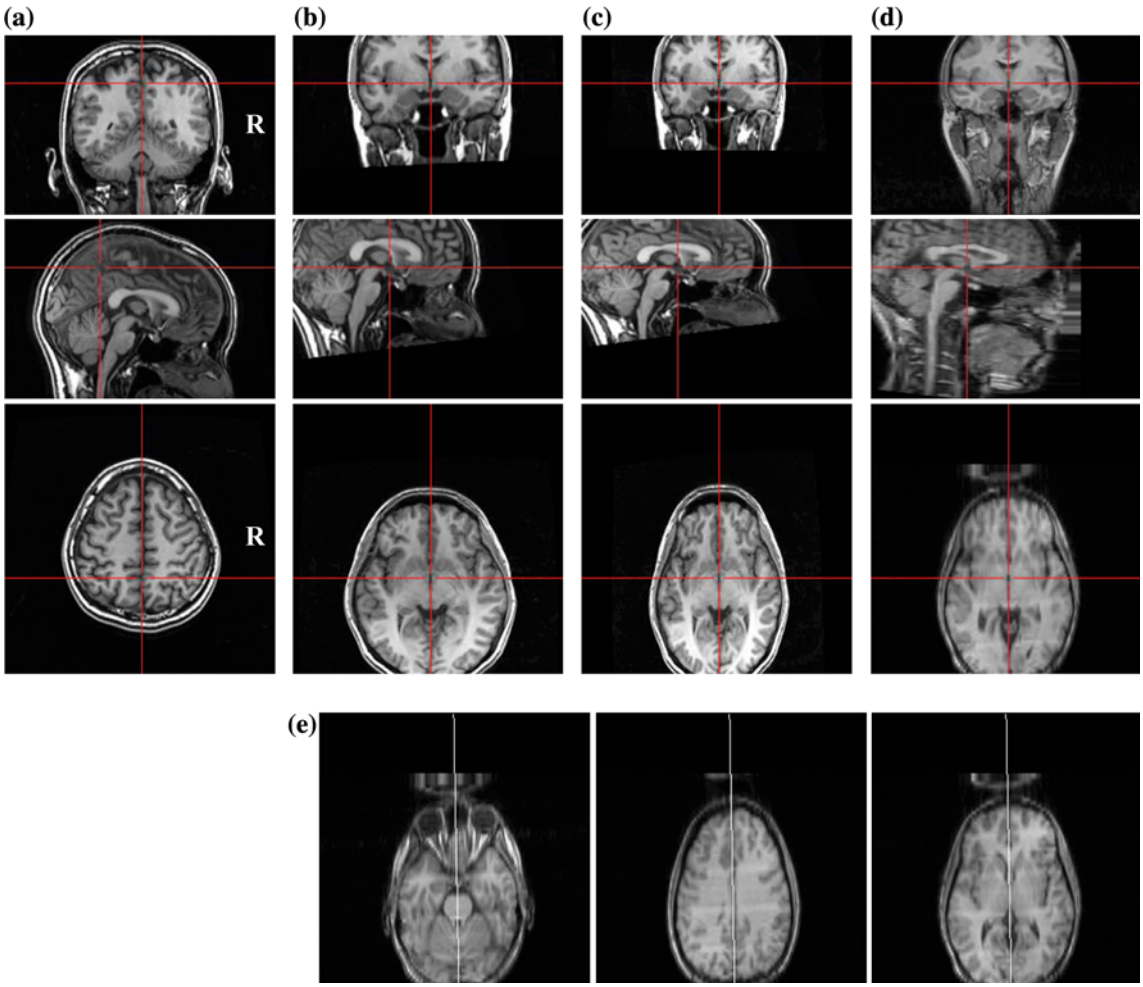

FIGURE 16. Affine registration for the brain images which include the neck regions and partial brain tissues are out of the field of view. (a) Source image. (b) Source image transformed using the estimated rigid parameters. (c) Affine registered source image. (d) Target image. (e) The estimated MSP of (d).

which apply registration intensively, such as VBM analysis. Some characteristics of the proposed method can greatly reduce the computational complexity. First, the adaptive placement decreases the number of the required RBFs. Second, coefficient estimation for one RBF at a time can greatly reduce the parameter search space and hence accomplish the registration task rapidly. In this way, the structure topology is always preserved in the modeling of deformation fields. Third, because of the compact support property of the Wendland's RBFs, there are only a few functions involved in the transformation calculation for each image point. Fourth, some implementation skills, such as the use of pyramid images and the lookup tables of the RBFs, are also quite beneficial to further improve the efficiency of image registration. Experimental results demonstrated that BIRT can accurately align brain images in a relatively short period of time compared with SPM2, HAMMER, and DARTEL.

The spatial normalization transforming MR brain images into the same stereotaxtic space for statistical comparison is an essential step in VBM analysis. It is commonly believed that the registration accuracy greatly affects the analysis results. However, to the best of our knowledge, there is still no quantitative study addressing this issue. Deviation of the VBM analysis was majorly contributed by the smoothing, the voxel-wise statistics, and the alignment errors of image registration. In this work, we constructed MR images of subjects with or without volume differences to investigate the registration errors upon the accuracy of VBM analysis. From the results of the well-controlled experiments, we conclude that an accurate registration method can facilitate VBM analysis to precisely report the structure differences between subject groups, in terms of both sensitivity and specificity.

BIRT can also be applied to register images of different modalities other than T1-weighted images. Our affine method is applicable to the alignment of brain images in which the MSP and CC have sufficiently large intensity contrast with the neighboring tissues. Additional preprocessing is required to invert the intensity contrast of brain tissues if the intensities in the MSP region are higher than those of CC. On the other hand, the proposed non-rigid registration method is general and suitable for the registration of images with similar structures.

In conclusion, we have proposed image registration, affine and non-rigid, which utilize the structure information derived from image derivatives. Experimental results indicated that the proposed BIRT methods can rapidly align brain structures with high accuracy compared to several other existing algorithms. An experiment using MR image groups with or without volume differences was also conducted to demonstrate that accurate registration can improve VBM analysis, in terms of both the sensitivity and the specificity.

ACKNOWLEDGMENTS

This work was supported in part by Taipei Veterans General Hospital, Taiwan, under Grants VGHUST-96-P1-05 and V97ER1-004, and National Science Council, Taiwan, under Grant NSC-98-2752-B-075-001-PAE.

REFERENCES

[1]Amit, Y. A nonlinear variational problem for image matching. *SIAM J. Sci. Comput.* 15:207–224, 1994.

[2]Arad, N., N. Dyn, D. Reisfeld, and Y. Yeshurun. Image warping by radial basis functions: application to facial expressions. *CVGIP-Graph Model Image Process.* 56:161–172, 1994.

[3]Ardekani, B. A., S. Guckemus, A. Bachman, M. J. Hoptman, M. Wojtaszek, and J. Nierenberg. Quantitative comparison of algorithms for inter-subject registration of 3D volumetric brain MRI scans. *J. Neurosci. Methods* 142:67–76, 2005.

[4]Ardekani, B. A., J. Kershaw, M. Braun, and I. Kanno. Automatic detection of the mid-sagittal plane in 3-D brain images. *IEEE Trans. Med. Imaging* 16:947–952, 1997.

[5]Ashburner, J. A fast diffeomorphic image registration algorithm. *NeuroImage* 38:95–113, 2007.

[6]Ashburner, J., J. L. R. Andersson, and K. J. Friston. High-dimensional image registration using symmetric priors. *NeuroImage* 9:619–628, 1999.

[7]Ashburner, J., and K. J. Friston. Nonlinear spatial normalization using basis functions. *Hum. Brain Mapp.* 7:254–266, 1999.

[8]Ashburner, J., and K. J. Friston. Voxel-based morphometry—the methods. *NeuroImage* 11:805–821, 2000.

[9]Ashburner, J., and K. J. Friston. Why voxel-based morphometry should be used. *NeuroImage* 14:1238–1243, 2001.

[10]Ashburner, J., P. Neelin, D. L. Collins, A. Evans, and K. Friston. Incorporating prior knowledge into image registration. *NeuroImage* 6:344–352, 1997.

[11]Bajcsy, R., and S. Kovačič. Multiresolution elastic matching. *Comput. Vis. Graph Image Process.* 46:1–21, 1989.

[12]Beyer, J. L., and K. R. R. Krishnan. Volumetric brain imaging findings in mood disorders. *Bipolar Disord.* 4:89–104, 2002.

[13]Bookstein, F. L. Principal warps: thin-plate splines and the decomposition of deformations. *IEEE Trans. Pattern Anal. Mach. Intell.* 11:567–585, 1989.

[14]Bookstein, F. L. "Voxel-based morphometry" should not be used with imperfectly registered images. *NeuroImage* 14:1454–1462, 2001.

[15]Brenneis, C., S. M. Bösch, M. Schocke, G. K. Wenning, and W. Poewe. Atrophy pattern in SCA2 determined by voxel-based morphometry. *NeuroReport* 14:1799–1802, 2003.

[16]Bro-Nielsen, M., and C. Gramkow. Fast fluid registration of medical images. *Lect. Notes Comput. Sci.* 1131:267–276, 1996.

[17]Cachier, P., E. Bardinet, D. Dormont, X. Pennec, and N. Ayache. Iconic feature based nonrigid registration: the PASHA algorithm. *Comput. Vis. Image Understand* 89:272–298, 2003.

[18]Camara, O., G. Delso, O. Colliot, A. Moreno-Ingelmo, and I. Bloch. Explicit incorporation of prior anatomical information into a nonrigid registration of thoracic and abdominal CT and 18-FDG whole-body emission PET images. *IEEE Trans. Med. Imaging* 26:164–178, 2007.

[19]Camara, O., J. A. Schnabel, G. R. Ridgway, W. R. Crum, A. Douiri, R. I. Scahill, D. L. G. Hill, and N. C. Fox. Accuracy assessment of global and local atrophy measurement techniques with realistic simulated longitudinal Alzheimer's disease images. *NeuroImage* 42:696–709, 2008.

[20]Camara, O., M. Schweiger, R. I. Scahill, W. R. Crum, B. I. Sneller, J. A. Schnabel, G. R. Ridgway, D. M. Cash, D. L. G. Hill, and N. C. Fox. Phenomenological model of diffuse global and regional atrophy using finite-element methods. *IEEE Trans. Med. Imaging* 25:1417–1430, 2006.

[21]Christensen, G. E., R. D. Rabbitt, and M. I. Miller. Deformable templates using large deformation kinematics. *IEEE Trans. Image Process.* 5:1435–1447, 1996.

[22]Chu, C., G. Tan, and J. Ashburner. Improving voxel-based morphometry with diffeomorphic non-linear registration by DARTEL toolbox: conventional SPM normalization vs. DARTEL normalization. In: 14th Annual Meeting of the Organization for Human Brain Mapping, Melbourne, Australia, 2008.

[23]Collignon, A., F. Maes, D. Delaere, D. Vandermeulen, P. Suetens, and G. Marchal. Automated multimodality medical image registration using information theory. In: Proceedings of the Information Processing in Medical Imaging, pp. 263–274, 1995.

[24]Collins, D. L., C. J. Holmes, T. M. Peters, and A. C. Evans. Automatic 3-D model-based neuroanatomical segmentation. *Hum. Brain Mapp.* 3:190–208, 1995.

[25]Collins, D. L., A. P. Zijdenbos, V. Kollokian, J. G. Sled, N. J. Kabani, C. J. Holmes, and A. C. Evans. Design and construction of a realistic digital brain phantom. *IEEE Trans. Med. Imaging* 17:463–468, 1998.

[26]Cootes, T. F., C. Beeston, G. J. Edwards, and C. J. Taylor. A unified framework for atlas matching using active appearance models. *Lect. Notes Comput. Sci.* 1613:322–333, 1999.

[27]Edwards, P. J., D. L. G. Hill, J. A. Little, and D. J. Hawkes. Deformation for image guided interventions using a three component tissue model. *Lect. Notes Comput. Sci.* 1230:218–231, 1997.

[28]Evans, A. C., D. L. Collins, S. R. Mills, E. D. Brown, R. L. Kelly, and T. M. Peters. 3D statistical neuroanatomical models from 305 MRI volumes. In: Nuclear Science Symposium and Medical Imaging Conference, San Francisco, CA, USA, Vol. 3, pp. 1813–1817, 1993.

[29]Evans, A. C., D. L. Collins, and B. Milner. An MRI-based stereotactic atlas from 250 young normal subjects. In: Society for Neuroscience (Abstract), Vol. 18, p. 408, 1992.

[30]Ferrant, M., A. Nabavi, B. Macq, F. A. Jolesz, R. Kikinis, and S. K. Warfield. Registration of 3-D intraoperative MR images of the brain using a finite-element biomechanical model. *IEEE Trans. Med. Imaging* 20:1384–1397, 2001.

[31]Fornefett, M., K. Rohr, and H. S. Stiehl. Radial basis functions with compact support for elastic registration of medical images. *Image Vis. Comput.* 19:87–96, 2001.

[32]Freeborough, P. A., and N. C. Fox. Modeling brain deformations in Alzheimer disease by fluid registration of serial 3D MR images. *J. Comput. Assist. Tomogr.* 22:838–843, 1998.

[33]Gholipour, A., N. Kehtarnavaz, R. Briggs, M. Devous, and K. Gopinath. Brain functional localization: a survey of image registration techniques. *IEEE Trans. Med. Imaging* 26:427–451, 2007.

[34]Good, C. D., I. Johnsrude, J. Ashburner, R. N. A. Henson, K. J. Friston, and R. S. J. Frackowiak. Cerebral asymmetry and the effects of sex and handedness on brain structure: a voxel-based morphometric analysis of 465 normal adult human brains. *NeuroImage* 14:685–700, 2001.

[35]Good, C. D., I. S. Johnsrude, J. Ashburner, R. N. A. Henson, K. J. Friston, and R. S. J. Frackowiak. A voxel-based morphometric study of ageing in 465 normal adult human brains. *NeuroImage* 14:21–36, 2001.

[36]Hellier, P., and C. Barillot. Coupling dense and landmark-based approaches for nonrigid registration. *IEEE Trans. Med. Imaging* 22:217–227, 2003.

[37]Hill, D. L. G., P. G. Batchelor, M. Holden, and D. J. Hawkes. Medical image registration. *Phys. Med. Biol.* 46:R1–R45, 2001.

[38]Jenkinson, M., P. Bannister, M. Brady, and S. Smith. Improved optimization for the robust and accurate linear registration and motion correction of brain images. *NeuroImage* 17:825–841, 2002.

[39]Jenkinson, M., and S. Smith. A global optimisation method for robust affine registration of brain images. *Med. Image Anal.* 5:143–156, 2001.

[40]Karacali, B., and C. Davatzikos. Simulation of tissue atrophy using a topology preserving transformation model. *IEEE Trans. Med. Imaging* 25:649–652, 2006.

[41]Karas, G. B., E. J. Burton, S. A. R. B. Rombouts, R. A. van Schijndel, J. T. O'Brien, P. Scheltens, I. G. McKeith, D. Williams, C. Ballard, and F. Barkhof. A comprehensive study of gray matter loss in patients with Alzheimer's disease using optimized voxel-based morphometry. *NeuroImage* 18:895–907, 2003.

[42]Kim, J. S., J. M. Lee, Y. H. Lee, J. S. Kim, I. Y. Kim, and S. I. Kim. Intensity based affine registration including feature similarity for spatial normalization. *Comput. Biol. Med.* 32:389–402, 2002.

[43]Kowalczyk, P., and M. Mrozowski. Mesh-free approach to Hemholtz equation based on radial basis functions. In: 15th International Conference on Microwave, Radar and Wireless Communication, Warsaw, Poland, pp. 702–705, 2004.

[44]Kybic, J., P. Thévenaz, A. Nirkko, and M. Unser. Unwarping of unidirectionally distorted EPI images. *IEEE Trans. Med. Imaging* 19:80–93, 2000.

[45]Lester, H., and S. R. Arridge. A survey of hierarchical non-linear medical image registration. *Pattern Recogn.* 32:129–149, 1999.

[46]Likar, B., and F. Pernuš. A hierarchical approach to elastic registration based on mutual information. *Image Vis. Comput.* 19:33–44, 2001.

[47]Little, J. A., D. L. G. Hill, and D. J. Hawkes. Deformations incorporating rigid structures. *Comput. Vis. Image Understand* 66:223–232, 1997.

[48]Liu, T. M., D. G. Shen, and C. Davatzikos. Deformable registration of cortical structures via hybrid volumetric and surface warping. *NeuroImage* 22:1790–1801, 2004.

[49]Liu, Y. X., R. T. Collins, and W. E. Rothfus. Robust midsagittal plane extraction from normal and pathological 3-D neuroradiology images. *IEEE Trans. Med. Imaging* 20:175–192, 2001.

[50]Marsland, S., C. J. Twining, and C. J. Taylor. Groupwise non-rigid registration using polyharmonic clamped-plate splines. *Lect. Notes Comput. Sci.* 2879:771–779, 2003.
[51]Mazziotta, J., A. Toga, A. Evans, P. Fox, J. Lancaster, K. Zilles, R. Woods, T. Paus, G. Simpson, B. Pike, C. Holmes, L. Collins, P. Thompson, D. MacDonald, M. Iacoboni, T. Schormann, K. Amunts, N. Palomero-Gallagher, S. Geyer, L. Parsons, K. Narr, N. Kabani, G. Le Goualher, D. Boomsma, T. Cannon, R. Kawashima, and B. Mazoyer. A probabilistic atlas and reference system for the human brain: international consortium for brain mapping (ICBM). *Phil. Trans. Roy. Soc. Lond. B Biol. Sci.* 356:1293–1322, 2001.
[52]Mazziotta, J. C., A. W. Toga, A. Evans, P. Fox, and J. Lancaster. A probabilistic atlas of the human brain—theory and rationale for its development. *NeuroImage* 2:89–101, 1995.
[53]Oatridge, A., J. Hajnal, and G. Bydder. Registration and Subtraction of Serial Magnetic Resonance Images of the Brain: Image Interpretation and Clinical Applications. CRC, Boca Raton, Florida: Medical Image Registration, 2001.
[54]Otsu, N. Threshold selection method from gray-level histograms. *IEEE Trans. Syst. Man. Cybern.* 9:62–66, 1979.
[55]Pluim, J. P. W., J. B. A. Maintz, and M. A. Viergever. Image registration by maximization of combined mutual information and gradient information. *IEEE Trans. Med. Imaging* 19:809–814, 2000.
[56]Pluim, J. P. W., J. B. A. Maintz, and M. A. Viergever. Interpolation artefacts in mutual information-based image registration. *Comput. Vis. Image Understand* 77:211–232, 2000.
[57]Pluim, J. P. W., J. B. A. Maintz, and M. A. Viergever. Mutual-information-based registration of medical images: a survey. *IEEE Trans. Med. Imaging* 22:986–1004, 2003.
[58]Press, W. H., S. A. Teukolsky, W. T. Vetterling, and B. P. Flannery. Numerical Recipes in C: The Art of Scientific Computing, 2nd edn. Cambridge, New York: Cambridge University Press, 1992.
[59]Rey, D., G. Subsol, H. Delingette, and N. Ayache. Automatic detection and segmentation of evolving processes in 3D medical images: application to multiple sclerosis. *Med. Image Anal.* 6:163–179, 2002.
[60]Roche, A., G. Malandain, X. Pennec, and N. Ayache. The correlation ratio as a new similarity measure for multimodal image registration. *Lect. Notes Comput. Sci.* 1496:1115–1124, 1998.
[61]Rohde, G. K., A. Aldroubi, and B. M. Dawant. The adaptive bases algorithm for intensity-based nonrigid image registration. *IEEE Trans. Med. Imaging* 22:1470–1479, 2003.
[62]Rueckert, D. Nonrigid registration: Concepts, Algorithms, and Applications. Medical Image Registration. Boca Raton, Florida: CRC, 2001.
[63]Rueckert, D., L. I. Sonoda, C. Hayes, D. L. G. Hill, M. O. Leach, and D. J. Hawkes. Nonrigid registration using free-form deformations: application to breast MR images. *IEEE Trans. Med. Imaging* 18:712–721, 1999.
[64]Ruprecht, D., R. Nagel, and H. Müller. Spatial free-form deformation with scattered data interpolation methods. *Comput. Graph* 19:63–71, 1995.
[65]Sermesant, M., C. Forest, X. Pennec, H. Delingette, and N. Ayache. Deformable biomechanical models: application to 4D cardiac image analysis. *Med. Image. Anal.* 7:475–488, 2003.
[66]Shen, D. G., and C. Davatzikos. HAMMER: hierarchical attribute matching mechanism for elastic registration. *IEEE Trans. Med. Imaging* 21:1421–1439, 2002.
[67]Smith, S., P. R. Bannister, C. Beckmann, M. Brady, S. Clare, D. Flitney, P. Hansen, M. Jenkinson, D. Leibovici, B. Ripley, M. Woolrich, and Y. Y. Zhang. FSL: new tools for functional and structural brain image analysis. *NeuroImage* 13:S249, 2001.
[68]Smith, S. M. Fast robust automated brain extraction. *Hum. Brain Mapp.* 17:143–155, 2002.
[69]Studholme, C., D. L. G. Hill, and D. J. Hawkes. An overlap invariant entropy measure of 3D medical image alignment. *Pattern Recogn.* 32:71–86, 1999.
[70]Talairach, J., and P. Tournoux. Co-Planar Stereotaxic Atlas of the Human Brain. New York: Thieme Medical Publishers, 1988.
[71]Thirion, J. P. Image matching as a diffusion process: an analogy with Maxwell's demons. *Med. Image Anal.* 2:243–260, 1998.
[72]Thompson, P. M., J. N. Gledd, R. P. Woods, D. MacDonald, A. C. Evans, and A. W. Toga. Growth patterns in the developing brain detected by using continuum mechanical tensor maps. *Nature* 404:190–193, 2000.
[73]Tuzikov, A. V., O. Colliot, and I. Bloch. Evaluation of the symmetry plane in 3D MR brain images. *Pattern Recogn. Lett.* 24:2219–2233, 2003.
[74]Twining, C. J., T. Cootes, S. Marsland, V. Petrovic, R. Schestowitz, and C. J. Taylor. A unified information-theoretic approach to groupwise non-rigid registration and model building. *Lect. Notes Comput. Sci.* 3565:1–14, 2005.
[75]Vercauteren, T., X. Pennec, A. Perchant, and N. Ayache. Non-parametric diffeomorphic image registration with the demons algorithm. *Lect. Notes Comput. Sci.* 4792:319–326, 2007.
[76]Viola, P., and W. M. Wells. Alignment by maximization of mutual information. *Int. J. Comput. Vis.* 24:137–154, 1997.
[77]Škrinjar, O., A. Nabavi, and J. Duncan. Model-driven brain shift compensation. *Med. Image Anal.* 6:361–373, 2002.
[78]Wendland, H. Piecewise polynomial, positive definite and compactly supported radial functions of minimal degree. *Adv. Comput. Math.* 4:389–396, 1995.
[79]Woods, R. P., S. T. Grafton, C. J. Holmes, S. R. Cherry, and J. C. Mazziotta. Automated image registration: I. General methods and intrasubject, intramodality validation. *J. Comput. Assist. Tomogr.* 22:139–152, 1998.
[80]Woods, R. P., S. T. Grafton, J. D. G. Watson, N. L. Sicotte, and J. C. Mazziotta. Automated image registration: II. Intersubject validation of linear and nonlinear models. *J. Comput. Assist. Tomogr.* 22:153–165, 1998.
[81]Wu, G. R., F. H. Qi, and D. G. Shen. Learning-based deformable registration of MR brain images. *IEEE Trans. Med. Imaging* 25:1145–1157, 2006.
[82]Zhang, Y. Y., M. Brady, and S. Smith. Segmentation of brain MR images through a hidden Markov random field model and the expectation-maximization algorithm. *IEEE Trans. Med. Imaging* 20:45–57, 2001.
[83]Zitová, B., and J. Flusser. Image registration methods: a survey. *Image Vis. Comput.* 21:977–1000, 2003.